drones

MDPI

Article

Quantifying Within-Flight Variation in Land Surface Temperature from a UAV-Based Thermal Infrared Camera

Jamal Elfarkh [1,2,*], Kasper Johansen [1], Victor Angulo [1], Omar Lopez Camargo [1] and Matthew F. McCabe [1,3]

[1] Hydrology, Agriculture and Land Observation (HALO) Laboratory, Division of Biological and Environmental Science and Engineering, King Abdullah University of Science and Technology (KAUST), Thuwal 23955-6900, Saudi Arabia; kasper.johansen@kaust.edu.sa (K.J.); victor.angulomorales@kaust.edu.sa (V.A.); omar.lopezcamargo@kaust.edu.sa (O.L.C.); matthew.mccabe@kaust.edu.sa (M.F.M.)

[2] Center for Remote Sensing Applications (CRSA), Mohammed VI Polytechnic University, Ben Guerir 43150, Morocco

[3] Climate and Livability Initiative, King Abdullah University of Science and Technology (KAUST), Thuwal 23955-6900, Saudi Arabia

* Correspondence: jamal.elfarkh@gmail.com

check for updates

Citation: Elfarkh, J.; Johansen, K.; Angulo, V.; Camargo, O.L.; McCabe, M.F. Quantifying Within-Flight Variation in Land Surface Temperature from a UAV-Based Thermal Infrared Camera. *Drones* **2023**, *7*, 617. https://doi.org/10.3390/drones7100617

Academic Editors: Diego González-Aguilera and Pablo Rodríguez-Gonzálvez

Received: 28 August 2023
Revised: 14 September 2023
Accepted: 17 September 2023
Published: 2 October 2023

Abstract: Land Surface Temperature (LST) is a key variable used across various applications, including irrigation monitoring, vegetation health assessment and urban heat island studies. While satellites offer moderate-resolution LST data, unmanned aerial vehicles (UAVs) provide high-resolution thermal infrared measurements. However, the continuous and rapid variation in LST makes the production of orthomosaics from UAV-based image collections challenging. Understanding the environmental and meteorological factors that amplify this variation is necessary to select the most suitable conditions for collecting UAV-based thermal data. Here, we capture variations in LST while hovering for 15–20 min over diverse surfaces, covering sand, water, grass, and an olive tree orchard. The impact of different flying heights and times of the day was examined, with all collected thermal data evaluated against calibrated field-based Apogee SI-111 sensors. The evaluation showed a significant error in UAV-based data associated with wind speed, which increased the bias from −1.02 to 3.86 °C for 0.8 to 8.5 m/s winds, respectively. Different surfaces, albeit under varying ambient conditions, showed temperature variations ranging from 1.4 to 6 °C during the flights. The temperature variations observed while hovering were linked to solar radiation, specifically radiation fluctuations occurring after sunrise and before sunset. Irrigation and atmospheric conditions (i.e., thin clouds) also contributed to observed temperature variations. This research offers valuable insights into LST variations during standard 15–20 min UAV flights under diverse environmental conditions. Understanding these factors is essential for developing correction procedures and considering data inconsistencies when processing and interpreting UAV-based thermal infrared data and derived orthomosaics.

Keywords: surface temperature variation; unmanned aerial vehicle; TIR camera sensitivity; meteorological factors

1. Introduction

Thermal infrared (TIR) remote sensing products collected from a range of satellite, airborne, and unmanned aerial vehicle (UAV) based platforms have contributed significantly to understanding the complex interactions between components of the surface–vegetation–atmosphere continuum [1]. Land-surface temperature (LST) represents one of the most informative variables in fields such as fire detection [2], hydrology [3] and precision agriculture [4,5]. In the agricultural sector, TIR data have gained considerable attention as an indicator of vegetation stress and plant water use [6,7]. In contrast to physiological indicators such as stomatal conductance or leaf water potential [8,9], remotely sensed TIR data provide a spatially extensive, rapid, and accurate means for assessing crop health and stress condition [10].

In the last decade, thermal sensors have seen significant improvement in their accuracy, weight, and size, making it possible to install a thermal camera onboard a UAV [11–13]. In parallel, UAV technology has become a mature means by which to collect information, especially where high spatial and temporal resolution information is required [14]. With advances in technology and reduction in cost, these platforms have become deployable by both the scientific community and individual enterprises. Given the range of information that can be retrieved from these platforms, one of the earliest application areas of UAVs was for agricultural field inspection and management. As a result, TIR data from UAVs have been successfully employed to detect crop water stress [15], monitor grain yield [16], estimate evapotranspiration [17], phenotype plants [18], and detect plant disease [19].

Although TIR data collected from UAV platforms have been widely utilized, with particular application in precision agriculture, the accuracy of UAV-mounted TIR sensors is an ongoing source of investigation [11,20–23]. Indeed, the miniaturization of TIR sensors to suit the payload limits of UAV platforms comes with an inherent compromise. Microbolometers are common sensors used in this miniaturization process to achieve low sensor weights, size reduction, and ease of integration, while also reducing production costs [24]. These sensors are "uncooled", meaning that they do not use a cooling system to maintain a stable and low internal temperature, but rather operate at the ambient temperature. While uncooled TIR sensors are less expensive and lighter than cooled sensors, they are also less accurate [25]. As the internal temperature of uncooled sensors is not stable, it affects the focal plane array temperature, which can produce incorrect and inconsistent readings of the target temperature [26]. Furthermore, during standard flights, the internal temperature of the sensor is more susceptible to change due to fluctuations in ambient temperature and wind drift [27].

Different protocols have been proposed to calibrate and correct uncooled sensor measurements. Mesas-Carrascosa et al. [25] proposed a drift correction approach for microbolometer sensors by utilizing redundant information from multiple overlapping images. Olbrycht and Więcek [28] introduced a novel approach to non-uniformity correction (NUC) in uncooled thermal cameras, utilizing a semi-transparent shutter to achieve thermal drift correction during thermal observation. Budzier and Gerlach [29] discussed the complexity of processing the uncooled TIR camera measurements and the mathematical and physical principles of calibration required for the non-uniformity correction, the temperature-dependent correction, the defective pixel correction, the shutter correction, and the radiometric calibration. Pestana et al. [30] proposed a melting-snow-based bias correction that reduced the root mean square error by about 1 °C for retrieving temperatures of water, forest, and snow surfaces. In a similar manner, Ribeiro-Gomes et al. [24], Torres-Rua [31], and Aragon et al. [11] used a black body reference to increase the absolute accuracy of UAV-based TIR data. Kelly et al. [27] argue that the camera stabilization and the effect of the ambient conditions on the TIR camera are the major causes of data uncertainty. Therefore, they proposed flight protocols to stabilize the camera and they highlighted the necessity of measuring the camera temperature in order to obtain robust radiometric calibration. Additionally, the emissivity, distance from the target, and atmospheric effects are other sources of error that are not well investigated and should be taken into account during UAV-based TIR data calibration [23,32,33].

Obtaining high spatial resolution data from UAVs generally limits the possibility of capturing large areas in one image, so an orthomosaic produced from hundreds or thousands of overlapping TIR images is used to cover larger areas at a high spatial resolution. While this approach is mature for reflectance-based optical image retrieval, for thermal data, there are additional complications. LST is a variable that keeps changing over time, given its response to factors such as wind speed, solar elevation, cloud cover, and land cover. The time needed for a UAV to cover the targeted area is linked to the extent of the area, flying height, speed, and the required forward and sideward overlap between the collected photos [34], and hence affects the LST variation that is likely to occur while mapping the target area. Given the thermal variability that can occur over short timespans and the difference in the image view angle of ground features between each overlapping image position (especially between neighbouring flight lines), the orthomosaic often includes a surface temperature bias due to temperature variations occurring during a UAV flight [13,18].

While previous studies have extensively examined LST variation across various time scales, ranging from seasonal to diurnal [35,36], our research addresses a crucial yet under-explored dimension: the assessment of LST variation over very short time intervals. Such precise data, vital for the collection and processing of UAV-derived information, has so far remained unexamined. Obtaining LST data with minimal variation necessitates a thorough investigation into the influence of environmental factors, land-cover characteristics, and the timing of UAV flights. In this study, LST variation was quantified over a standard UAV flight duration of 15–20 min. This research seeks to enhance our comprehension of thermal variability that may arise during UAV flights and potentially impact the accuracy of UAV-based thermal mapping. To do this, we collected and analysed UAV data from various surfaces, environments, and different times of the day. Additionally, we investigated the influence of meteorological and environmental factors that can contribute to observed variations in LST, which can aid in determining optimal timing and conditions for collecting UAV-based thermal images. To assess the LST variation, the UAV was set to hover over a fixed point while collecting images every 120 ms for the duration of the life of the batteries (15–20 min). This investigation not only enriches our understanding of the complexities involved in generating an accurate orthomosaic of LST from collected UAV thermal data but also forms the foundation for the development of advanced algorithms tailored to accommodate the intricacies of LST variation in data processing.

2. Materials and Methods

2.1. Description of the Study Sites

The experiment was undertaken in two locations in Saudi Arabia (Figure 1). The first was at the King Abdullah University of Science and Technology (KAUST) (22.31° N, 39.09° E), where UAV-based TIR data were collected over sand, water, and grass. The climate at this site is tropical and arid with an annual rainfall of <100 mm and average air temperatures (T_a) of about 20 °C in winter and 37 °C in summer. The second site was a large olive tree farm (>8 million trees) in Al-Jouf, northern Saudi Arabia (Figure 1) (29.82° N, 38.31° E). Here, the olive trees are planted in rows with a spacing of about 1.5 m between trees and 4 m between rows, and irrigated using a drip system. Al-Jouf is also located in a tropical, arid climate with an annual rainfall of <100 mm [35] with an average T_a of about 10 °C in winter and exceeding 40 °C in summer.

2.2. Data Collection

At the KAUST site, multiple UAV flights were conducted over each land-cover type (sand, water, and grass) at different heights (20, 50, and 100 m) on 24 March 2022 (see Table 1). All hovering UAV flights were planned with UgCS v.4.18 software (SPH Engineering, Riga, Latvia) to ensure that the UAV was hovering in the same position at the three flight heights for each of the three land-cover types. A DJI Matrice 100 quadcopter (Da Jiang Innovations, Shenzhen, China) was used to collect TIR imagery from a nadir view angle using a FLIR Tau 2 core radiometric thermal camera (TeAx, Wilnsdorf, Germany). The camera has a weight of 95 g, a 13 mm focal length, and a resolution of 640 × 512 pixels. The sensor collects TIR images across the 7.5–13.5 μm spectral range. While its absolute temperature accuracy is about 5 °C, its thermal precision is much higher at about 0.04 °C [11,13]. The camera collects TIR images at an image frequency of 8.33 Hz (i.e., one image every ~120 ms). Raw DN images were extracted as 16-bit TIFF radiance image files using the ThermoViewer 2.0 software (Fluke Process Instruments) after the TeAx data acquisition.

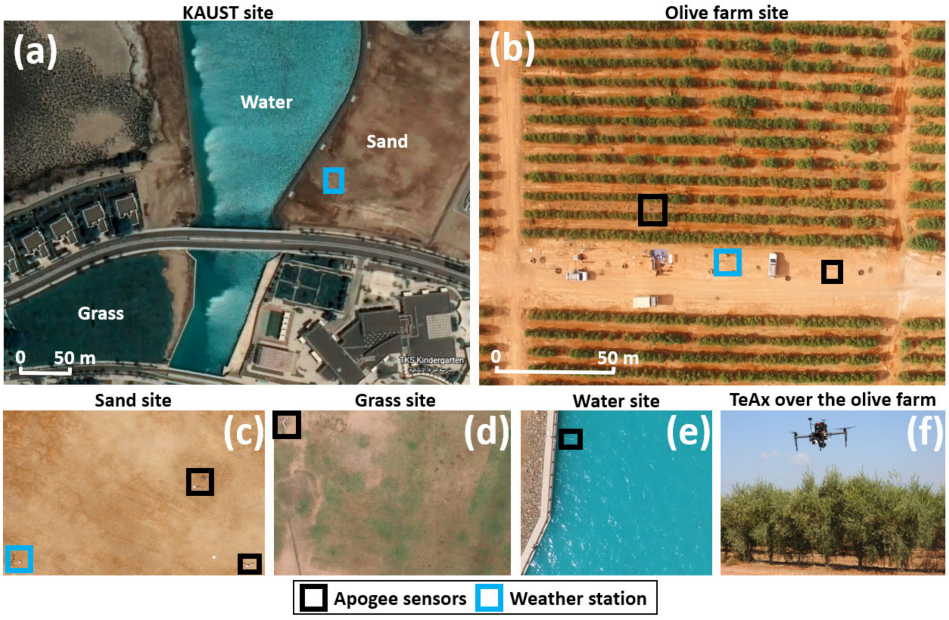

Figure 1. (**a**) Image of the King Abdullah University of Science and Technology (KAUST) site in Saudi Arabia (from Google Earth) showing the location of the sand (**c**), grass (**d**), and water (**e**) sites. Image collected from the UAV (**f**) of the olive farm (**b**) located in Al-Jouf, Saudi Arabia. The black and blue squares show the location of the Apogee sensors and the weather stations, respectively.

Table 1. Flight times and meteorological conditions, including air temperature, wind speed, and solar radiation recorded during each UAV flight survey on 24 November 2020 and 24 March 2022.

Date	Site		Flight Height (m)	Starting Time	Flight Duration (min)	Air Temperature (°C)	Absolute Humidity (g/m^3)	Wind Speed (m/s)	Net Radiation (W/m^2)
24 November 2020	Olive farm		100	09:49	18	18.0	5.37	0.9	91.2
			100	13:45	17	22.5	7.03	1.2	277.2
			100	17:14	16	20.5	9.08	0.4	59.0
24 March 2022	KAUST	Sand	20	12:10	19	22.5	11.69	8.2	692.8
			50	11:45	18	22.4	11.78	8.3	683.9
			100	11:14	19	22.2	11.94	8.3	658.2
		Water	20	14:07	18	22.7	11.88	9.1	604.7
			50	13:44	18	22.7	12.05	9.2	637.6
			100	13:12	18	22.7	11.94	8.4	672.9
		Grass	20	15:34	19	22.6	11.86	8.5	380.1
			50	15:12	17	22.8	11.89	8.2	448.5
			100	14:48	16	22.7	12.15	8.6	516.1

At the KAUST sites, four Apogee SI-111 infrared radiometers (Apogee Instruments Inc., Logan, UT, USA) were installed to verify the accuracy of the TIR data collected by the TeAx camera. The Apogee sensors have a broadband spectral range that spans from 8 to 14 µm, with a measurement range from −60 to 110 °C, an operating temperature range from −40 to 80 °C, and a manufacturer accuracy of ±0.5 °C. Two Apogee sensors were directed toward the surface, i.e., sand, water, and grass, while two other sensors were measuring the temperature of a black panel to assess the camera accuracy over a near-perfect emittance surface. The Apogee sensors were set up for each land-cover type to make sure they were located approximately in the centre of the UAV TIR photos when hovering to reduce impacts from any potential vignetting effects.

At the olive farm, three hovering UAV flights were undertaken over the same area at the same height (100 m) on 24 November 2020. The three flights were undertaken at 10 a.m., 2 p.m., and 5:30 p.m., ensuring a large range of surface temperatures and net radiation values (Table 1). Two Apogee sensors were installed in the olive tree farm: one over olive trees deemed representative in terms of tree structure (height, size, leaf density) and the second over bare soil to validate the thermal TeAx data. While the UAV flights on 24 March 2022 were all collected during mostly clear sky conditions, some stratocumulus and cirrostratus clouds were present over the olive farm. To improve the interpretation of the thermal UAV data collected for the olive tree farm, we acquired a simultaneous red-green-blue (RGB) video for all three UAV flights from the same UAV platform using a Zenmuse X3 camera (Dà-Jiāng Innovations, Shenzhen, China).

A weather station was set up at both the KAUST and olive farm sites to measure wind speed, wind direction, temperature, and radiation (Table 1). The average recorded wind speeds at the KAUST site exceeded 8 m/s, while the air temperature remained steady throughout the experiment. The net radiation was relatively steady during the flights for the sand and water land-cover types, while the radiation started to decrease in the afternoon when the flights over a grass field were undertaken. The weather station at the olive farm recorded low wind speeds on 24 November 2020, while net radiation varied considerably between each of the three flights (Table 1).

2.3. Apogee Sensor Calibration

In order to evaluate the accuracy of the TIR images collected by the TeAx camera, Apogee sensors were used to measure the surface temperature continuously at 1 min intervals, with measurements recorded on DataTaker DT80M loggers (Thermofisher Scientific Inc., Waltham, MA, USA). The Apogee sensors were initially calibrated in the factory but can be biased, as reported by Aragon et al. [11]. To ensure reliable evaluation of the TeAx images, all Apogee sensors used in this study were calibrated in an environmental chamber based on the approach proposed by Aragon et al. [11]. The calibration of the Apogee sensors was performed inside an environment chamber where the ambient temperature was set to 10, 15, 20, 25, 30, 35, and 40 °C, respectively, for different black body temperatures. One by one, six sensors were placed at a fixed distance of 8 cm from a black body. The temperature of the black body was fixed at different temperatures including 20, 30, 40, 50, and 60 °C. Based on the temperature values recorded by the Apogee sensors and the one recorded by the black body at different ambient temperatures, a linear regression equation (Equation (1)) was established for each sensor taking into consideration the sensor measurement ($T_{measured}$) and the ambient temperature (T_a). The coefficients obtained for each Apogee sensor used are presented in the Results section.

$$T_{corrected} = T_{measured} \times a_1 + T_a \times a_2 + a_3 \quad (1)$$

2.4. Calibration and Evaluation of TeAx Data

The approach developed by Aragon et al. [11] was applied to the raw TIR images for post-flight processing, where a matrix was produced for all the pixels of the TeAx photos to apply a calibration function. This calibration is necessary to reduce vignette effects and increase measurement accuracy. The same calibration method was also applied to the Apogee sensors. In an environmental chamber, the relationship between the TeAx camera measurements of each pixel and the corresponding black body temperatures, which are considered the same for the complete black body surface, was determined at various ambient temperatures. Based on this relationship, a multilinear regression matrix was established to calibrate all the thermal images captured by the camera while hovering.

In order to compare the TeAx and the Apogee sensor measurements, an average of 3×3 representative pixels from the area covered by the Apogee sensors was selected (black squares in Figure 1). The size of the pixels chosen vary in each flight due to the varying UAV hovering height (i.e., 20, 50, and 100 m). In this study, the Apogees were installed at around 1 m height above each surface, which produced a footprint of approximately 0.4 m^2 based on the 22° field of view. The UAV-based thermal images collected at the same time as the Apogee measurements, i.e., once every 1 min, were selected for comparison. On the olive farm, the comparison between the TeAx and the Apogee data was performed over two locations: one over olive trees and the other over bare soil (Figure 1b). The interpretation of the temperature variations over the soil and the trees was carried out separately.

Similarly, Apogee sensors were used for the three surfaces at the KAUST site. At the sand and grass sites, a black panel was used to evaluate the camera accuracy. Due to a technical issue, the Apogee measurements at the grass field site were only collected at 50 and 100 m height (not at 20 m) over the black panel and at 100 m over a patch of grass. The same pixels chosen in the TeAx images to be compared with the Apogee sensor measurements were used to track the surface temperature variation for the different flights. For the assessment of LST variation, an image collected every 30 s was selected.

To assess the calibration performance of the Apogee sensors and the comparison between the TeAx and the Apogee sensor measurements, the root mean square error ($RMSE$), the bias and the coefficient of determination (R^2) were calculated.

$$RMSE = \sqrt{\frac{1}{n}\sum_{i=1}^{n}(y_i - x_i)^2} \quad (2)$$

$$bias = \frac{1}{n}\sum_{i=1}^{n}(y_i - x_i) \quad (3)$$

$$R^2 = \left(\frac{\sum(x_i - x)(y_i - y)}{\sqrt{\sum(x_i - x)^2\sum(y_i - y)^2}}\right)^2 \quad (4)$$

where x_i is the measured values, y_i is the estimated values, and n is the number of observations.

3. Results

3.1. Apogee Calibration

The comparison of the surface temperature values measured by the Apogee sensors in the environmental chamber over a black body against its recorded temperature values showed a linear correlation with an R^2 of 0.99 for all sensors before and after calibration (Figure 2 and Table 2). However, before the calibration, a significant bias of 2.82 °C and RMSE of 2.96 °C were computed. The bias and RMSE were reduced to approximately 0 °C and 0.19 °C, respectively, after the calibration (Figure 2b). As can be seen in Table 3, the calibration coefficients for each Apogee sensor were different, indicating that each sensor requires separate calibration.

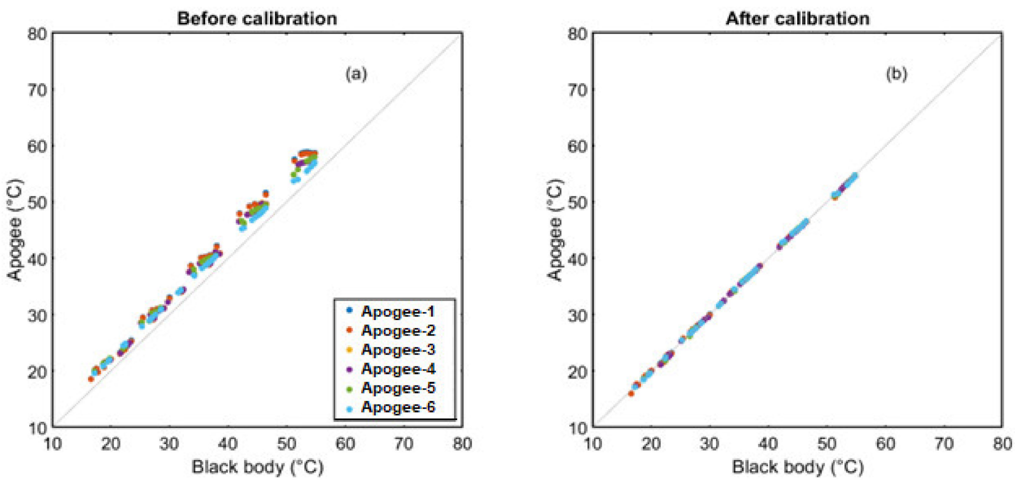

Figure 2. Comparison between the Apogee sensor measurements and the temperatures recorded of the black body before (**a**) and after (**b**) the calibration.

Table 2. Root mean square error (*RMSE*), coefficient of determination (R^2), and bias of the relationship between Apogee measurements and black body temperature before and after calibration.

b	Before Calibration			After Calibration		
Apogee Name	**RMSE (°C)**	**R^2**	**Bias (°C)**	**RMSE (°C)**	**R^2**	**Bias (°C)**
Apogee-1	3.13	0.994	2.87	0.22	0.999	7.39×10^{-15}
Apogee-2	3.20	0.994	2.93	0.18	0.999	-2.40×10^{-14}
Apogee-3	2.40	0.999	2.39	0.19	0.999	-3.25×10^{-15}
Apogee-4	3.03	0.995	2.90	0.16	0.999	8.75×10^{-15}
Apogee-5	3.06	0.998	3.00	0.21	0.999	6.80×10^{-16}
Apogee-6	2.98	0.996	2.86	0.17	0.999	-7.35×10^{-15}

Table 3. Calibration equation coefficients for the Apogee sensors.

Apogee Name	a_1	a_2	a_3
Apogee-1	0.8977	0.0886	−1.5405
Apogee-2	0.8935	0.0928	−1.5535
Apogee-3	1.0005	0.0031	−2.4901
Apogee-4	0.9238	0.0714	−1.8514
Apogee-5	0.9587	0.0389	−2.3875
Apogee-6	0.9263	0.0677	−1.8137

3.2. Apogees/TeAx Comparison

TeAx camera measurements over the four field sites, i.e., bare sandy soil, water, grass, and olive trees were evaluated against the field-based Apogee measurements. When comparing the TeAx TIR data collected at various heights (20, 50, and 100 m) with the Apogee sensor measurements taken over a black panel at the sand and grass sites (Figure 3), the results were better (RMSE = 0.73–4.12 °C) than those obtained over the sandy, water, and grass surfaces (RMSE = 2.89–4.58 °C) at the three altitudes (Figure 4). The larger error in the observed surface temperatures of sand, water, and grass may be attributed to the variation in temperature uniformity of the surfaces. The black panels exhibit a more uniform temperature distribution within the Apogee sensor footprint than the other surfaces, which have more variability due to differences in colour and roughness. Therefore, the average LST pixel value of the black panel is expected to be more similar to the Apogee sensor measurement than the average pixel value of the other surfaces with a more heterogeneous composition.

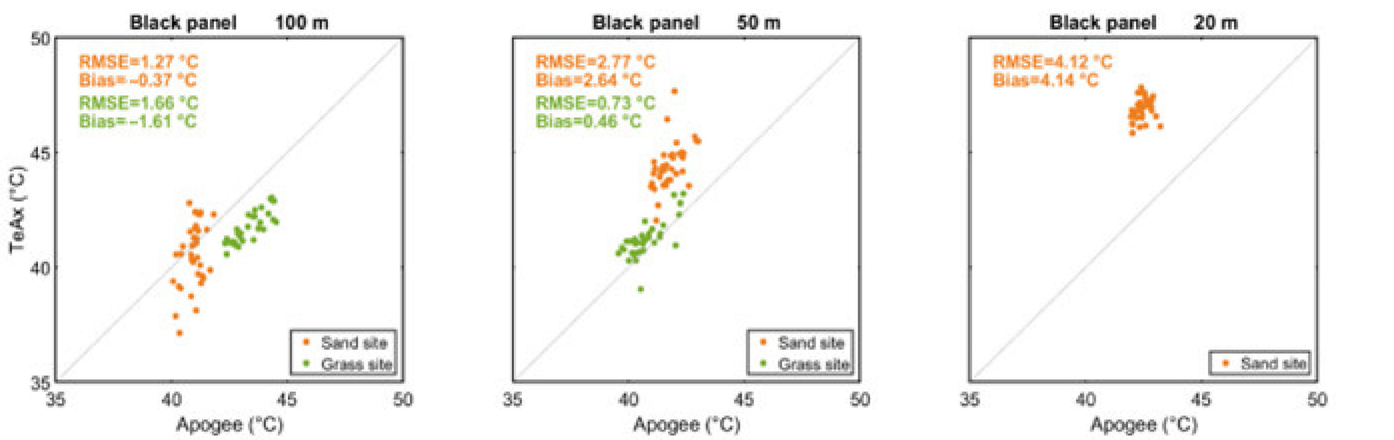

Figure 3. Scatterplots of the relationships between the TeAx and Apogee measurements over the black panels at the sand and grass sites at 20, 50, and 100 m of height.

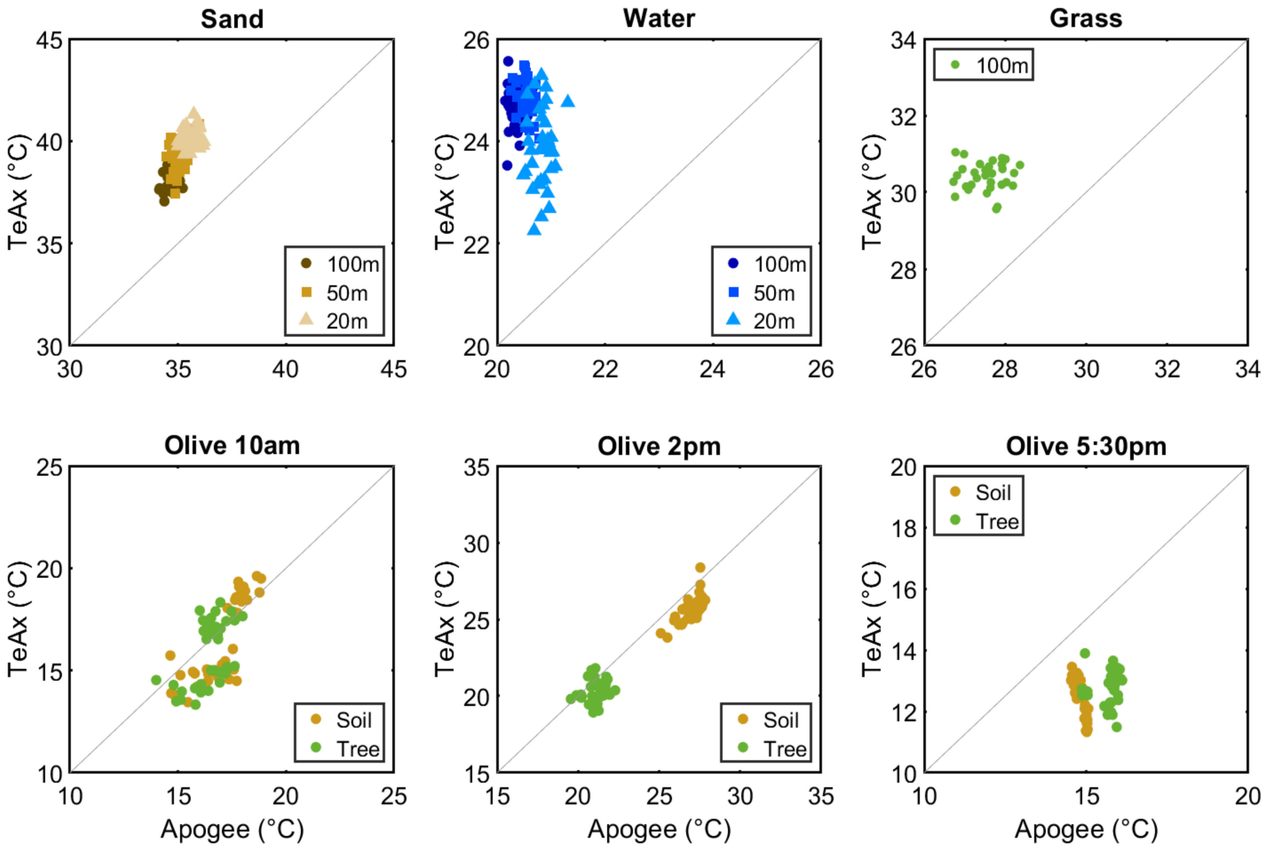

Figure 4. Comparison between the TeAx (average of 3 × 3 representative pixels from the area covered by the Apogee sensors) and the Apogee sensor measurements over sand and water at 20, 50, and 100 m height and grass at 100 m and over olive trees at different times (10 am, 2 p.m. and 5:30 p.m.) of the same day.

The comparison between the TeAx camera and the Apogee sensor measurements over the four surfaces shows that the TeAx camera performed better over the olive trees than at the other sites, with an overall RMSE and bias of 2.24 °C and −1.02 °C, respectively, and an RMSE and bias ranging from 2.89 °C to 4.58 °C and from 2.88 °C to 4.55 °C, respectively, for the other sites (Figure 4 and Table 4). The difference in the TeAx performance can be linked to the effect of the wind speed. All the flights over the sand, water, and grass sites took place on the same day, when the average wind speed was 8.5 m/s as opposed to a recorded wind speed average of 0.8 m/s during the UAV data capture at the olive tree farm. Wind speed is one of the factors that can affect the surface temperature of an uncooled thermal sensor the most [13] and the accuracy of the camera measurements can be influenced by the wind speed at both the hovering height and at ground level. Kelly et al. [27] tested the effect of a sustained wind speed of 2 and 3.3 m/s under laboratory conditions and found that the wind speed has an impact on the correlation between the digital number from the camera and the surface temperature. Similarly, Virtue et al. [22] and Wan et al. [23] reported that the wind could contribute to an uncertainty of several degrees when measuring LST using TIR cameras. The grass site examined in this study was surrounded by buildings and palm trees, potentially causing a decrease in wind speed. This reduction in wind speed resulted in relatively low RMSE and bias values of 2.89 °C and 2.88 °C, respectively. However, it is essential to note that the weather station measurements (Table 1) did not reflect the lower wind speed at the grass site, since the station remained situated at the more exposed sand site throughout the experiment conducted on 24 March 2022.

Table 4. Root mean square error (RMSE) and bias of the relationships between the TeAx camera (average of 3 × 3 representative pixels from the area covered by the Apogee sensors) and Apogee measurements over sand, water, grass, and olive trees.

Flights		**RMSE (°C)**	**Bias (°C)**
Sand	20 m	4.58	4.55
	50 m	4.43	4.44
	100 m	3.54	3.56
Water	20 m	3.13	3.04
	50 m	4.30	4.29
	100 m	4.32	4.31
Grass	100 m	2.89	2.88
Olive 10 a.m.	Soil	1.34	−0.42
	Tree	1.45	−0.59
Olive 2 p.m.	Soil	1.44	−1.33
	Tree	1.11	−0.80
Olive 5:30 p.m.	Soil	2.51	−2.38
	Tree	2.98	−2.91

The flights at the olive farm site occurred throughout the day, i.e., 09:49, 13:45, and 17:14, during which predominant meteorological conditions changed. Across the three flights, the recorded absolute humidity was 5.37, 7.03, and 9.08 g/m^3 at 09:49, 13:45, and 17:14, respectively, which might explain the higher RMSEs (2.51 °C for soil and 2.98 °C for trees) at 17:14 compared to the RMSEs (1.34 °C and 1.44 °C for soil and 1.45 °C and 1.11 °C for trees) at 09:49 and 13:45, respectively. Absolute humidity represents the water volume in the atmosphere and can affect the amount of absorbed radiation, which influences the amount of thermal radiation received by the sensor [36,37]. This can lead to confounding influences on the temperature measurements, especially if the radiometer is not able to distinguish between the thermal radiation emitted by the surface and the radiation emitted by the atmosphere or reflected by nearby objects. Thus, atmospheric corrections with low relative humidity when capturing UAV-based thermal data may improve LST estimates [31].

3.3. TeAx Measurements Variation

For the 16–19 min duration of each of the 12 UAV flights (three at each of the four sites), the UAV was hovering over the same position. Over the four sites (olive trees, sand, water and grass), the temperature variation (maximum minus minimum of the same pixels used in the Apogee/TeAx comparison) ranged between 1.4 and 6 °C (Figure 5). The flight over the olive farm at 10 a.m. showed the highest variation (i.e., 5 °C for trees and 6 °C for soil), which is linked to the fast increase in solar radiation at this time of the day. At 2 p.m., the LST was expected to be more stable but the plots in Figure 5 show a LST variation of around 3 °C for trees and 4 °C for soil. These fluctuations in LST can be linked to the presence of cirrostratus clouds (rather than wind effects), which affected the solar radiation reaching the surface for parts of the flight. For the Olive-5:30 p.m. flight, both soil and trees temperatures show an increase in LST at 5:19 p.m., which was attributed to the shadows from stratocumulus clouds that dissipated during this period.

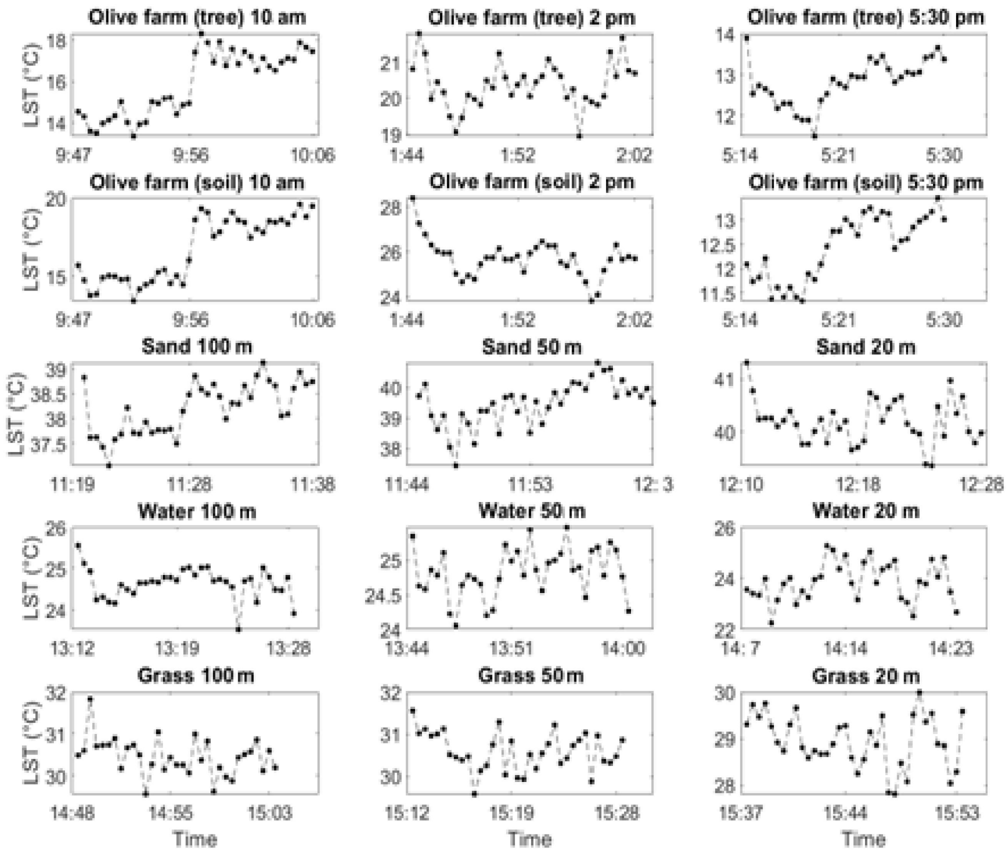

Figure 5. Timeseries of the surface temperature of the same pixels (3 × 3 pixels) presented in Figure 4 at 30 s intervals measured by the TeAx camera over the olive farm (trees and soil) at 10 a.m., 2 p.m., and 5:30 p.m. of the same day and over sand, water, and grass at 20, 50, and 100 m of height.

At the KAUST sites, LST variation was between 1.5 and 3 °C in all nine flights, presenting significant fluctuations that were probably induced by the high wind speed. The elevated wind speed can generate variations in LST through a range of mechanisms. For instance, advection occurs when the wind brings in warmer or colder air, resulting in an increase or decrease in LST for a particular area. Additionally, wind-enhanced evaporation accelerates surface cooling by facilitating faster heat dissipation [38]. The lowest TeAx-recorded LST variation occurred during the Sand-20 m, Water-100 m, and Water-50 m flights (with a range of 2 °C, 2 °C, and 1.5 °C, respectively) between 12 and 2 p.m., when the solar radiation reached its maximum and the surface temperature plateaued.

Similar to the timeseries presented in Figure 5, the maps in Figure 6 show the temporal variation in the surface temperature measured by the TeAx camera. It can be seen that the temperature variation at each site is not uniform across the imaged extent, with some zones depicting more variation than others. This spatial difference in the temperature variation is specifically present in the Olive-5:30 p.m. flight and in the Sand-100 m flight. Around sunset in the olive farm (the Olive-5:30 p.m. flight), some parts of the site varied from 8 to 15 °C, while other parts showed temperature variations as small as 1 °C during the hovering flight. For the same flight, the images of the olive farm can be divided into two parts, i.e., a soil part (black) and an arboreal part (red). The difference in the LST values between soil and trees was low at 5 p.m. compared to that observed at 10 a.m. and 2 p.m. However, the soil temperature cooled down earlier than the trees, possibly due to irrigation, which was initiated approximately 2 h prior to the UAV flight at 17:14, causing the wet soil to absorb heat energy, which helps to reduce the temperature of the surface. Additionally, irrigation can also keep the soil cool via evaporation, thereby reducing the amount of sensible heat that is transferred to the atmosphere. This is supported by the observed decrease in air temperature, which reached 20.5 °C, and an increase in absolute humidity, which reached 9.08 g/m^3 at 17:14, compared to midday when they were 22.5 °C and 7.03 g/m^3, respectively. For the Sand-100 m flight, a spatial difference in the temperature variation was observed between different parts of the extent captured. The northwestern part of the imaged area shows larger temperature variations (35 to 40 °C) than the southeastern part of the image, which varied from 40 to 42 °C during the whole flight. That northwestern part was very close to the water, which might explain the warming delay in this part, especially considering that the wind was coming from the water towards the sandy area with an average wind direction of 328°.

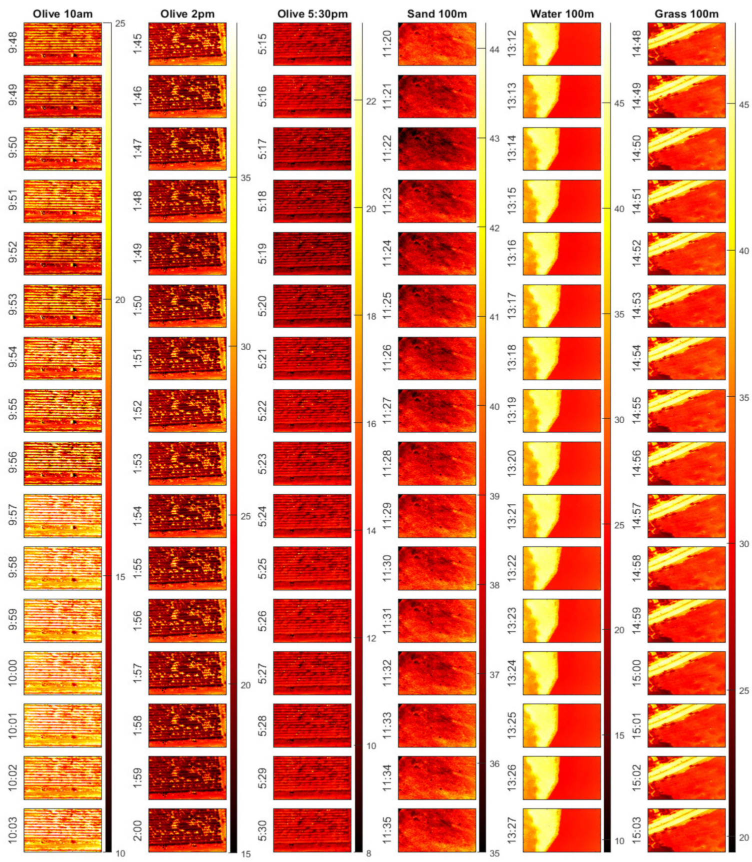

Figure 6. Spatiotemporal variation in the surface temperature measured by the TeAx camera over olive trees at 10 a.m., 2 p.m., and 5:30 p.m. of the same day and over sand, water, and grass at 100 m of height.

Figures 5 and 6 illustrate that the temperature variation at each observed location does not follow a consistent monotonic pattern. Furthermore, in certain instances, the temperature can fluctuate by more than 1 °C within a minute. This variability can cause major issues when producing UAV-based orthomosaics of LST. To further investigate these temporal variations, we calculated the difference (ΔLST) between the maximum and minimum LST values within different time intervals (1 s, 5 s, 15 s, 30 s, 1 min, 5 min, and 10 min) for each flight (see Figure 7). The average of ΔLST obtained within each specific time interval shows an expected increase as the time interval lengthens. However, even within a short time range of one second, ΔLST can reach relatively high values (>0.5 °C), as indicated by the blue dots in Figure 7. Additionally, the figure reveals that the ΔLST values do not increase linearly with time. For example, there are instances where relatively high ΔLST (e.g., 1 °C) occurred during a 5 s interval, while other intervals of 15 s exhibited ΔLST values below 0.5 °C. This irregular increase in ΔLST over time is particularly noticeable during the 5 min interval, where different ΔLST values were obtained, especially in the Olive-10 am and Water-100 m flights.

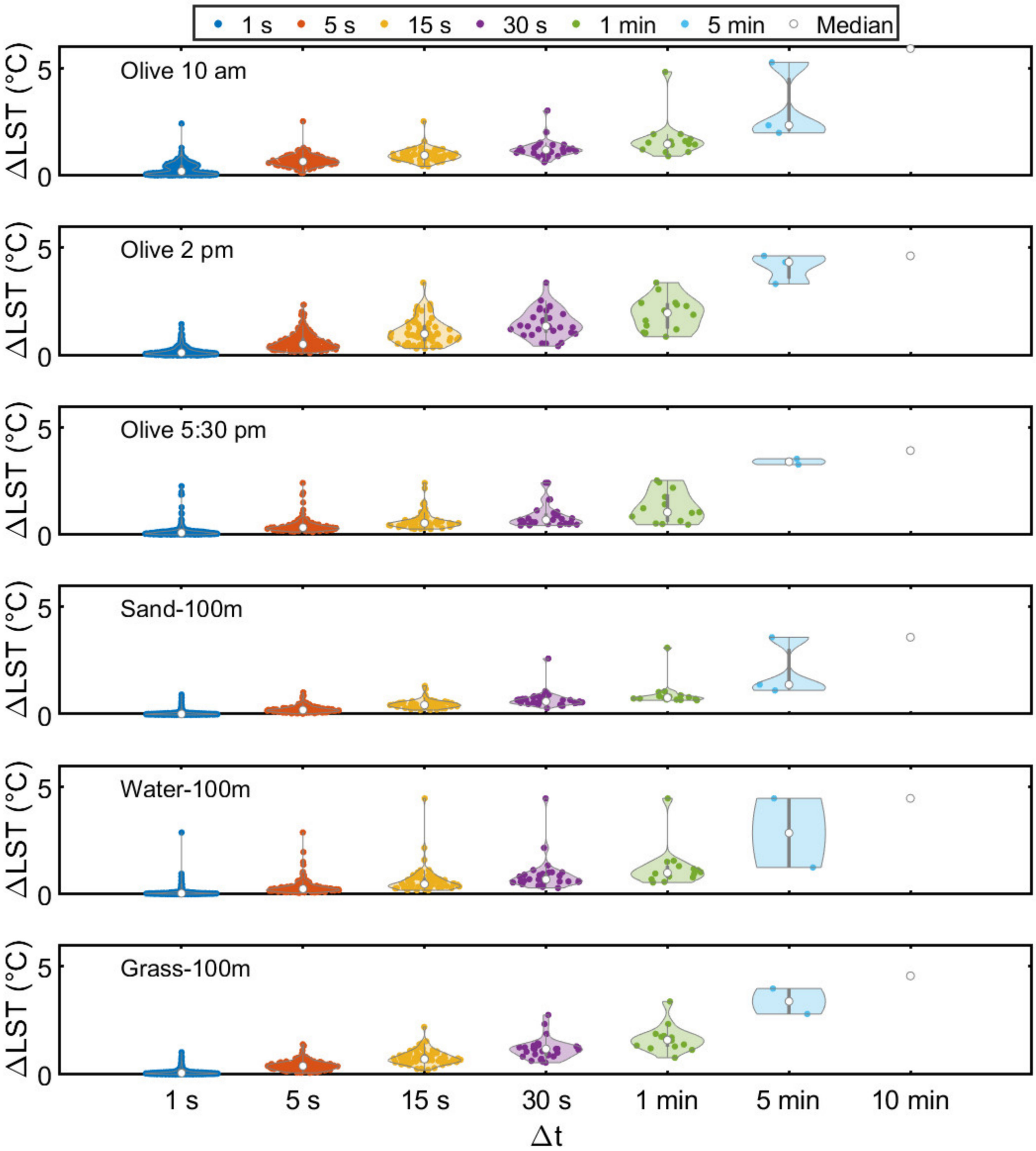

Figure 7. Variation in LST (maximum–minimum) during different time ranges (1, 5, 15, and 30 s and 1, 5, and 10 min).

To explore the factors behind the variation in LST, the concurrently measured meteorological factors were examined. As meteorological data were only collected once every minute, the variation in each variable, including LST, wind speed (WS), net radiation (Rn), air humidity (RH) and air temperature (Ta), was calculated each minute as the difference between the registered value (observed every minute) and the average of all measurements during the flight time. Figures 8 and 9 show the correlations between the variation calculated for LST and the variation calculated for the meteorological variables. The results show that when the LST variation was low, its correlation with the meteorological variables variability was weak. In contrast, when the LST variation exceed ±1 °C, a greater correlation was observed, especially with Rn and WS variations during flights such as Sand-100 m, Sand-50 m, and Grass-100 m. The correlations with Rn variation were positive, yielding a correlation coefficient (R) between 0.4 and 0.5, in contrast to WS variation, where the correlations were negative, with an R between −0.4 and −0.3. Overall, LST variation was mostly affected by Rn variation, albeit with greater fluctuations in LST variation than observed for net radiation. Part of these fluctuations can be related to the WS variation, particularly large wind gusts. The fluctuations in Rn can be affected by the diurnal cycle of the sun position or the presence of clouds that impact the amount of sunlight reaching the surface. In addition, soil moisture is a key factor that can significantly affect the variation in LST. In areas with high soil moisture, the solar energy absorbed by the surface is used for the evaporation of water, which is a latent energy process, resulting in minimal temperature variation. On the other hand, in areas with low soil moisture, solar radiation is transformed into sensible energy, leading to an increase in surface temperature. Moreover, soil moisture increases the heat capacity of the soil and thus, it takes longer to cool or warm the soil surface. In agricultural fields, the influence of soil moisture on the variation in LST becomes more pronounced due to its spatial heterogeneity, particularly during irrigation events. Identifying the factors generating LST variation is not straightforward, since these factors can interact with one another, making it challenging to predict LST variation accurately.

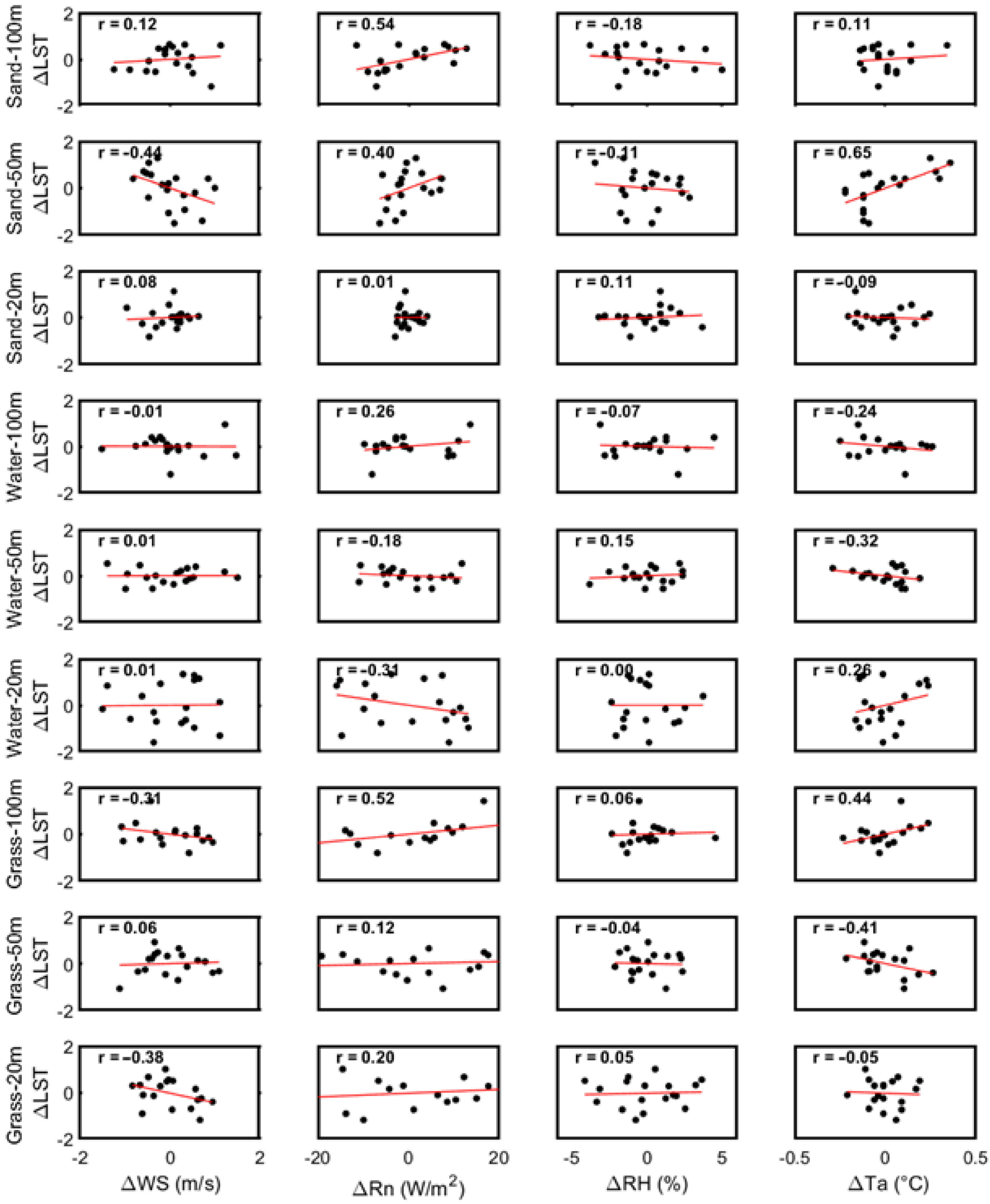

Figure 8. Relationship between the LST variation $\left(\Delta LST = LST_i - \overline{LST}\right)$, calculated as the observation value at one point in time minus the average value of all observations during each flight, and the variation in meteorological variables (WS: wind speed, Rn: net radiation, RH: air humidity and Ta: air temperature) at the KAUST site.

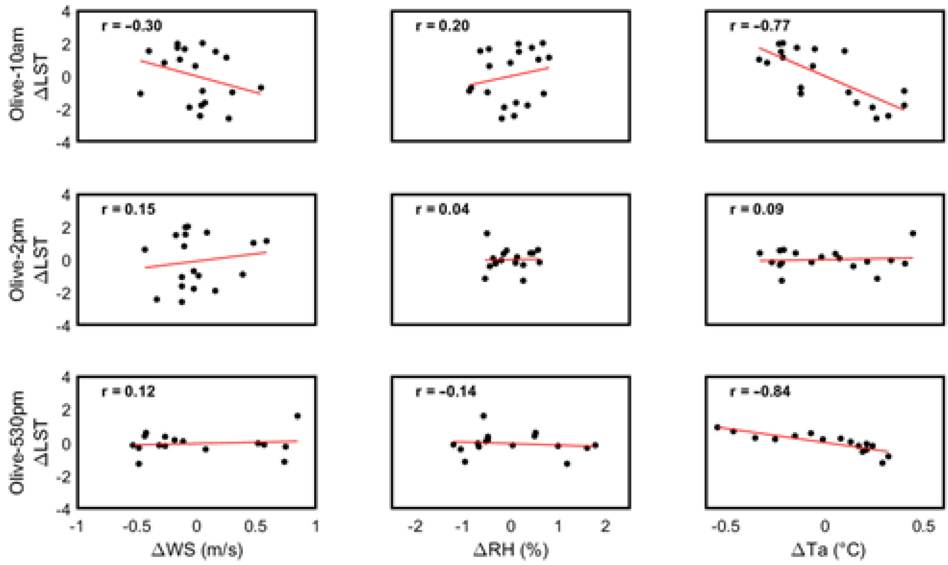

Figure 9. Relationship between the LST variation $\left(\Delta LST = LST_i - \overline{LST}\right)$, calculated as the observation value at one point in time minus the average value of all observations during each flight, and the variation in meteorological variables (WS: wind speed, RH: air humidity and Ta: air temperature) at the olive farm site.

4. Discussion

Measuring surface temperature remotely has always posed a challenge given the dynamic relationship of this variable with multiple environmental factors. Additionally, the properties of the target (mainly the emissivity) and the characteristics of the sensor often limit the feasibility of collecting consistent and accurate LST measurements. UAV-based platforms provide an opportunity to assess LST at field scales with a high spatio-temporal resolution. Several studies have focused on evaluating the accuracy of UAV-based thermal data, including the impact of environmental factors such as temperature and wind speed on the uncooled sensors used in these platforms [23,39]. The use of cooled thermal sensors is a potential solution, which has previously not been practical due to the payload restrictions of UAV platforms. However, new, miniaturized, and lightweight cooled thermal imaging cores are becoming available, which will reduce the effect of the ambient temperature and the wind drift when collecting thermal data (see https://tecotec.com.vn/en/cooled-thermal-imaging-core/, (accessed on 16 September 2023)). External shutters have also been developed to increase the accuracy of absolute temperature measurements (see https://thermalcapture.com/extended-value-external-shutter-for-flir-vue-pro-r/, (accessed on 16 September 2023)). Virtue et al. [22] modified an uncooled thermal infrared sensor with a proprietary external heated shutter as a calibration source. Their findings indicate that the use of this heated shutter enhanced thermal measurements, resulting in more consistent and accurate LST data. Future studies should test these latest innovations in UAV-based thermal imaging to quantify improvements in observed absolute thermal measurements and determine their suitability for orthomosaic generation.

In our study, we analysed the effects of environmental factors on a timeseries of UAV-based thermal data to assess LST variability during a standard UAV flight of 15–20 min to understand how the LST data co-varied with wind speed, direction, atmospheric conditions, radiance, and solar elevation, measured by a weather station. The results showed that in windy conditions, the accuracy of LST measurements is low (Figure 4 and Table 4) no matter what the hovering height is, which aligns with previous research findings [13,27]. Differences between the LST measurements obtained via the UAV and the ground-truth data were found to be affected by the uncooled thermal sensor's sensitive to sudden or large changes in wind speed. Additionally, the accuracy of the UAV measurements is reduced by the atmospheric water content, which is represented in this study by the absolute humidity (Figure 4 and Table 4). This accuracy reduction occurs due to the absorption of surface-emitted thermal radiation towards the sensor, which highlighted the need for an atmospheric correction even at low altitudes as reported by Torres-Rua [31] and Wu et al. [40].

Although UAV-based thermal data is a promising tool for various applications, the lack of consistency due to environmental factors affecting measurements of LST remains a concern, especially when an accuracy less than 1 °C is required, which is often the case for precision agricultural applications [25,41]. In addition, the considerable fluctuation of LST within brief timeframes makes the processing and implementation of thermal data more challenging for standard orthomosaicking approaches. Indeed, the variation in LST may restrict the utilization of thermal data collected by UAVs in various applications. For example, the temporal representativeness of LST values is reduced due to this variability, thereby limiting the use of UAV-based LST orthomosaics in contextual algorithms used for detecting crop stress [7] or estimating evapotranspiration [42]. These algorithms are based on the relation between the end members, i.e., cold and hot pixels, present in the orthomosaic and the values of each pixel. However, the variation in LST through the duration of a UAV flight covering a targeted surface area can also affect the end members, causing them to change simultaneously. This means that considering a single end member's value for the entire image-data capture may provide incorrect information about each pixel's state compared to the rest of the orthomosaic.

Regarding the generation of a LST orthomosaic, the observed variation in LSTs may complicate the identification of matching points during the dense point-cloud generation and hence decrease the quality of the orthorectification. In addition, the generation of an orthomosaic from different frames of LST can be affected by this variation, and the extent of this impact depends on the blending method used. The three methods proposed in the Agisoft Metashape 2.0.3 software (mosaic, average, and disabled) or the one suggested by Malbéteau et al. [13] each handle temperature variations differently. The mosaic and average methods involve the calculation of each pixel value by averaging different values from multiple overlapping frames, which are captured at different times, especially between neighbouring flight lines. In contrast, the disabled method preserves the individual characteristics of each image and assigns the pixel value of the closest image to nadir. Therefore, the impact of temperature variation is more significant in the mosaic and average methods than in the disabled method. Acorsi et al. [20] tested these three blending modes and reported that the disabled mode shows the best performance, with an RMSE of 3.08 °C, compared to the mosaic and the average modes, with an RMSE of 3.93 °C and 3.14 °C, respectively. To minimize the effect of temperature variation in the orthomosaic, the disabled method may be the best option, as it assigns a single value to each pixel and preserves the original characteristics of each image. However, the disabled method may generate an orthomosaic with abrupt temperature variations, whereas the mosaic and average methods produce an orthomosaic depicting smoother LST variations. The mosaic and averaging methods may reduce noise and increase the overall image quality when environmental conditions are optimal, i.e., stable solar radiation, low wind speed, and cloud-free conditions. Malbéteau et al. [13] proposed a method different to the three aforementioned where they combined each flight line, creating individual swaths instead of computing the entire image dataset at once. Subsequently, they joined the swaths by applying a correction for bias between swaths due to flight direction. This method reduced wind effects between neighbouring swaths obtained from opposing flight directions and enabled an assessment of temperature inconsistencies between adjacent overlapping orthophotos within a swath due to LST variation. However, this swath-based method corrects the wind effects on the sensor onboard the UAV and not the effects on the surface. The wind can rapidly change the surface properties, producing LST variation, e.g., due to changes in the form, position, and orientation of leaves in crop fields. As LST variations were assessed from hovering flights in our study, it should be noted that the impact of flight direction on LST measurements, as assessed by Malbéteau et al. [13], is an additive effect not evaluated herein.

Identifying the ideal environmental conditions to collect thermal data is required not just to ensure accurate LST measurements but also to minimize fluctuations over time during flights. Our findings indicate that variations are primarily attributed to sun exposure, with morning fluctuations of 6 °C compared to 2 °C at midday within our study areas. Additionally, cloud coverage affects the amount of solar radiation reaching the surface, resulting in rapid fluctuations in LST values, even due to thin cirrus clouds, which were present during one of the hovering flights over the olive tree plantation. LST fluctuations are more pronounced at higher wind speeds, especially in areas with heterogeneous land cover, such as surfaces in close proximity to water, as exemplified in the Sand-100 m flight, where the cool air over the water lowers the temperature of the surrounding surfaces (Figure 6). For crop fields, irrigation is a critical factor to consider when selecting the flight time, given the rapid change not just in the wet fraction of the soil but also in the transpiration process that cools down the plants [43–45]. Overall, it can be challenging to identify the causes responsible for generating LST variation because these factors often interact with one another in complex ways.

5. Conclusions

UAV TIR data were collected from a fixed hovering position over different land cover types and at different altitudes. The TeAx TIR camera was compared to calibrated Apogee sensors, and the results showed the sensitivity of the thermal camera to wind speed, where the bias ranged from −1.02 °C to 3.86 °C at wind speeds of 0.8 m/s and 8.5 m/s, respectively. The images collected over four sites (i.e., bare sandy soil, water, grass, and olive trees) showed an LST variation between 1.4 and 6 °C during a single UAV flight of 16–19 min. The lowest variation was registered at midday when the solar radiation was more stable compared to the morning and afternoon. However, the presence of thin clouds impacted solar radiation, leading to notable variations in LST, even at midday. Additionally, collecting data across areas with diverse land cover increases the LST variation, particularly for surfaces near water that are influenced by advection fluxes. While this study provides new insights into the temporal variation in UAV-based LST and environmental factors affecting LST, further research is required to test new lightweight cooled thermal sensors and understand the effect of rapid LST variation in applications such as crop stress detection and evapotranspiration estimation.

Author Contributions: Conceptualization, J.E., K.J. and M.F.M.; methodology, J.E., K.J. and M.F.M.; software, J.E.; validation, J.E., K.J. and M.F.M.; formal analysis, J.E., K.J. and M.F.M.; investigation, J.E., K.J., V.A., O.L.C. and M.F.M.; resources, J.E., K.J., V.A., O.L.C. and M.F.M.; data curation, J.E., K.J., V.A., O.L.C. and M.F.M.; writing—original draft preparation, J.E.; writing—review and editing, J.E., K.J., V.A., O.L.C. and M.F.M.; visualization, J.E.; supervision, K.J. and M.F.M.; project administration, M.F.M.; funding acquisition, M.F.M. All authors have read and agreed to the published version of the manuscript.

Funding: Research reported in this publication was supported by the King Abdullah University of Science and Technology (KAUST).

Data Availability Statement: Not applicable.

Acknowledgments: The authors wish to thank Javier Blanco Sacristán for reviewing and providing insightful comments, which have improved the quality of this work.

Conflicts of Interest: The authors declare no conflict of interest.

References

1. Coutts, A.M.; Harris, R.J.; Phan, T.; Livesley, S.J.; Williams, N.S.G.; Tapper, N.J. Thermal infrared remote sensing of urban heat: Hotspots, vegetation, and an assessment of techniques for use in urban planning. *Remote Sens. Environ.* **2016**, *186*, 637–651. [CrossRef]
2. Wang, T.; Wang, Y.; Zhao, F.; Feng, H.; Liu, J.; Zhang, L.; Zhang, N.; Yuan, G.; Wang, D. A spatio-temporal temperature-based thresholding algorithm for underground coal fire detection with satellite thermal infrared and radar remote sensing. *Int. J. Appl. Earth Obs. Geoinform.* **2022**, *110*, 102805. [CrossRef]
3. Baker, E.A.; Lautz, L.K.; McKenzie, J.M.; Aubry-Wake, C. Improving the accuracy of time-lapse thermal infrared imaging for hydrologic applications. *J. Hydrol.* **2019**, *571*, 60–70. [CrossRef]
4. Khanal, S.; Fulton, J.; Shearer, S. An overview of current and potential applications of thermal remote sensing in precision agriculture. *Comput. Electron. Agric.* **2017**, *139*, 22–32. [CrossRef]
5. Messina, G.; Modica, G. Applications of UAV Thermal Imagery in Precision Agriculture: State of the Art and Future Research Outlook. *Remote. Sens.* **2020**, *12*, 1491. [CrossRef]
6. Santesteban, L.G.; Di Gennaro, S.F.; Herrero-Langreo, A.; Miranda, C.; Royo, J.B.; Matese, A. High-resolution UAV-based thermal imaging to estimate the instantaneous and seasonal variability of plant water status within a vineyard. *Agric. Water Manag.* **2017**, *183*, 49–59. [CrossRef]
7. Stutsel, B.; Johansen, K.; Malbéteau, Y.M.; McCabe, M.F. Detecting Plant Stress Using Thermal and Optical Imagery From an Unoccupied Aerial Vehicle. *Front. Plant Sci.* **2021**, *12*, 734944. [CrossRef]
8. Goto, K.; Yabuta, S.; Ssenyonga, P.; Tamaru, S.; Sakagami, J.-I. Response of leaf water potential, stomatal conductance and chlorophyll content under different levels of soil water, air vapor pressure deficit and solar radiation in chili pepper (*Capsicum chinense*). *Sci. Hortic.* **2021**, *281*, 109943. [CrossRef]
9. Yan, H.; Shah, S.S.; Zhao, W.; Liu, F. Variations in water relations, stomatal characteristics, and plant growth between quinoa and pea under salt-stress conditions. *Pak. J. Bot.* **2019**, *52*, 1–7. [CrossRef]
10. Zhou, Z.; Majeed, Y.; Naranjo, G.D.; Gambacorta, E.M. Assessment for crop water stress with infrared thermal imagery in precision agriculture: A review and future prospects for deep learning applications. *Comput. Electron. Agric.* **2021**, *182*, 106019. [CrossRef]
11. Aragon, B.; Johansen, K.; Parkes, S.; Malbeteau, Y.; Al-Mashharawi, S.; Al-Amoudi, T.; Andrade, C.F.; Turner, D.; Lucieer, A.; McCabe, M.F. A Calibration Procedure for Field and UAV-Based Uncooled Thermal Infrared Instruments. *Sensors* **2020**, *20*, 3316. [CrossRef] [PubMed]
12. Deane, S.; Avdelidis, N.P.; Ibarra-Castanedo, C.; Zhang, H.; Nezhad, H.Y.; Williamson, A.A.; Mackley, T.; Maldague, X.; Tsourdos, A.; Nooralishahi, P. Comparison of Cooled and Uncooled IR Sensors by Means of Signal-to-Noise Ratio for NDT Diagnostics of Aerospace Grade Composites. *Sensors* **2020**, *20*, 3381. [CrossRef] [PubMed]
13. Malbéteau, Y.; Johansen, K.; Aragon, B.; Al-Mashhawari, S.K.; McCabe, M.F. Overcoming the Challenges of Thermal Infrared Orthomosaics Using a Swath-Based Approach to Correct for Dynamic Temperature and Wind Effects. *Remote. Sens.* **2021**, *13*, 3255. [CrossRef]
14. Chen, S.; Laefer, D.F.; Mangina, E. State of Technology Review of Civilian UAVs. *Recent Patents Eng.* **2016**, *10*, 160–174. [CrossRef]
15. Gonzalez-Dugo, V.; Zarco-Tejada, P.; Nicolás, E.; Nortes, P.A.; Alarcón, J.J.; Intrigliolo, D.S.; Fereres, E. Using high resolution UAV thermal imagery to assess the variability in the water status of five fruit tree species within a commercial orchard. *Precis. Agric.* **2013**, *14*, 660–678. [CrossRef]
16. Elsayed, S.; Elhoweity, M.; Ibrahim, H.H.; Dewir, Y.H.; Migdadi, H.M.; Schmidhalter, U. Thermal imaging and passive reflectance sensing to estimate the water status and grain yield of wheat under different irrigation regimes. *Agric. Water Manag.* **2017**, *189*, 98–110. [CrossRef]
17. Nieto, H.; Kustas, W.P.; Torres-Rua, A.; Alfieri, J.G.; Gao, F.; Anderson, M.C.; White, W.A.; Song, L.; del Mar Alsina, M.; Prueger, J.H.; et al. Evaluation of TSEB turbulent fluxes using different methods for the retrieval of soil and canopy component temperatures from UAV thermal and multispectral imagery. *Irrig. Sci.* **2019**, *37*, 389–406. [CrossRef]
18. Perich, G.; Hund, A.; Anderegg, J.; Roth, L.; Boer, M.P.; Walter, A.; Liebisch, F.; Aasen, H. Assessment of Multi-Image Unmanned Aerial Vehicle Based High-Throughput Field Phenotyping of Canopy Temperature. *Front. Plant Sci.* **2020**, *11*, 150. [CrossRef]
19. Granum, E.; Pérez-Bueno, M.L.; Calderón, C.E.; Ramos, C.; de Vicente, A.; Cazorla, F.M.; Barón, M. Metabolic responses of avocado plants to stress induced by Rosellinia necatrix analysed by fluorescence and thermal imaging. *Eur. J. Plant Pathol.* **2015**, *142*, 625–632. [CrossRef]
20. Acorsi, M.G.; Gimenez, L.M.; Martello, M. Assessing the Performance of a Low-Cost Thermal Camera in Proximal and Aerial Conditions. *Remote Sens.* **2020**, *12*, 3591. [CrossRef]
21. Döpper, V.; Gränzig, T.; Kleinschmit, B.; Förster, M. Challenges in UAS-Based TIR Imagery Processing: Image Alignment and Uncertainty Quantification. *Remote Sens.* **2020**, *12*, 1552. [CrossRef]
22. Virtue, J.; Turner, D.; Williams, G.; Zeliadt, S.; McCabe, M.; Lucieer, A. Thermal Sensor Calibration for Unmanned Aerial Systems Using an External Heated Shutter. *Drones* **2021**, *5*, 119. [CrossRef]
23. Wan, Q.; Brede, B.; Smigaj, M.; Kooistra, L. Factors Influencing Temperature Measurements from Miniaturized Thermal Infrared (TIR) Cameras: A Laboratory-Based Approach. *Sensors* **2021**, *21*, 8466. [CrossRef] [PubMed]

24. Ribeiro-Gomes, K.; Hernández-López, D.; Ortega, J.F.; Ballesteros, R.; Poblete, T.; Moreno, M.A. Uncooled Thermal Camera Calibration and Optimization of the Photogrammetry Process for UAV Applications in Agriculture. *Sensors* **2017**, *17*, 2173. [CrossRef]
25. Mesas-Carrascosa, F.-J.; Pérez-Porras, F.; de Larriva, J.E.M.; Frau, C.M.; Agüera-Vega, F.; Carvajal-Ramírez, F.; Martínez-Carricondo, P.; García-Ferrer, A. Drift Correction of Lightweight Microbolometer Thermal Sensors On-Board Unmanned Aerial Vehicles. *Remote Sens.* **2018**, *10*, 615. [CrossRef]
26. Nugent, P.W.; Shaw, J.A.; Pust, N.J. Correcting for focal-plane-array temperature dependence in microbolometer infrared cameras lacking thermal stabilization. *Opt. Eng.* **2013**, *52*, 061304. [CrossRef]
27. Kelly, J.; Kljun, N.; Olsson, P.-O.; Mihai, L.; Liljeblad, B.; Weslien, P.; Klemedtsson, L.; Eklundh, L. Challenges and Best Practices for Deriving Temperature Data from an Uncalibrated UAV Thermal Infrared Camera. *Remote Sens.* **2019**, *11*, 567. [CrossRef]
28. Olbrycht, R.; Więcek, B. New approach to thermal drift correction in microbolometer thermal cameras. *Quant. Infrared Thermogr. J.* **2015**, *12*, 184–195. [CrossRef]
29. Budzier, H.; Gerlach, G. Calibration of uncooled thermal infrared cameras. *J. Sensors Sens. Syst.* **2015**, *4*, 187–197. [CrossRef]
30. Pestana, S.; Chickadel, C.C.; Harpold, A.; Kostadinov, T.S.; Pai, H.; Tyler, S.; Webster, C.; Lundquist, J.D. Bias Correction of Airborne Thermal Infrared Observations Over Forests Using Melting Snow. *Water Resour. Res.* **2019**, *55*, 11331–11343. [CrossRef]
31. Torres-Rua, A. Vicarious Calibration of sUAS Microbolometer Temperature Imagery for Estimation of Radiometric Land Surface Temperature. *Sensors* **2017**, *17*, 1499. [CrossRef]
32. Aubrecht, D.M.; Helliker, B.R.; Goulden, M.L.; Roberts, D.A.; Still, C.J.; Richardson, A.D. Continuous, long-term, high-frequency thermal imaging of vegetation: Uncertainties and recommended best practices. *Agric. For. Meteorol.* **2016**, *228–229*, 315–326. [CrossRef]
33. Hammerle, A.; Meier, F.; Heinl, M.; Egger, A.; Leitinger, G. Implications of atmospheric conditions for analysis of surface temperature variability derived from landscape-scale thermography. *Int. J. Biometeorol.* **2016**, *61*, 575–588. [CrossRef] [PubMed]
34. Pepe, M.; Fregonese, L.; Scaioni, M. Planning airborne photogrammetry and remote-sensing missions with modern platforms and sensors. *Eur. J. Remote Sens.* **2018**, *51*, 412–436. [CrossRef]
35. Xiang, Y.; Ye, Y.; Peng, C.; Teng, M.; Zhou, Z. Seasonal variations for combined effects of landscape metrics on land surface temperature (LST) and aerosol optical depth (AOD). *Ecol. Indic.* **2022**, *138*, 108810. [CrossRef]
36. Malbéteau, Y.; Parkes, S.; Aragon, B.; Rosas, J.; McCabe, M.F. Capturing the Diurnal Cycle of Land Surface Temperature Using an Unmanned Aerial Vehicle. *Remote Sens.* **2018**, *10*, 1407. [CrossRef]
37. El Kenawy, A.M.; McCabe, M.F. A multi-decadal assessment of the performance of gauge- and model-based rainfall products over Saudi Arabia: Climatology, anomalies and trends. *Int. J. Climatol.* **2015**, *36*, 656–674. [CrossRef]
38. Rosas, J.; Houborg, R.; McCabe, M.F. Sensitivity of Landsat 8 Surface Temperature Estimates to Atmospheric Profile Data: A Study Using MODTRAN in Dryland Irrigated Systems. *Remote Sens.* **2017**, *9*, 988. [CrossRef]
39. Allred, B.; Martinez, L.; Fessehazion, M.K.; Rouse, G.; Koganti, T.; Freeland, R.; Eash, N.; Wishart, D.; Featheringill, R. Time of day impact on mapping agricultural subsurface drainage systems with UAV thermal infrared imagery. *Agric. Water Manag.* **2021**, *256*, 107071. [CrossRef]
40. Song, D.; Zhang, X.; Zhou, X.; Shi, X.; Jin, X. Influences of wind direction on the cooling effects of mountain vegetation in urban area. *Build. Environ.* **2021**, *209*, 108663. [CrossRef]
41. Song, B.; Park, K. Verification of Accuracy of Unmanned Aerial Vehicle (UAV) Land Surface Temperature Images Using In-Situ Data. *Remote Sens.* **2020**, *12*, 288. [CrossRef]
42. Wu, Y.; Shan, Y.; Lai, Y.; Zhou, S. Method of calculating land surface temperatures based on the low-altitude UAV thermal infrared remote sensing data and the near-ground meteorological data. *Sustain. Cities Soc.* **2022**, *78*, 103615. [CrossRef]
43. Kustas, W.P.; Norman, J.M. Use of remote sensing for evapotranspiration monitoring over land surfaces. *Hydrol. Sci. J.* **1996**, *41*, 495–516. [CrossRef]
44. Elfarkh, J.; Simonneaux, V.; Jarlan, L.; Ezzahar, J.; Boulet, G.; Chakir, A.; Er-Raki, S. Evapotranspiration estimates in a traditional irrigated area in semi-arid Mediterranean. Comparison of four remote sensing-based models. *Agric. Water Manag.* **2022**, *270*, 107728. [CrossRef]
45. Zhao, W.; Dong, X.; Wu, Z.; Wei, C.; Li, L.; Yu, D.; Fan, X.; Ma, Y. Using infrared thermal imaging technology to estimate the transpiration rate of citrus trees and evaluate plant water status. *J. Hydrol.* **2022**, *615*, 128671. [CrossRef]